


# Immersion infrared reflection-absorption spectroscopy studies on diamond-like carbon surfaces. I. Formation of electrophilic groups on surfaces of amorphous carbon films aging in ambient air

Claus-Peter Klages<sup>1</sup>  | Ralf Bandorf<sup>2</sup> | Holger Gerdes<sup>2</sup> | Antje Jung<sup>1</sup> | Vitaly Raev<sup>1</sup>

<sup>1</sup>Institute for Surface Technology, IOT, Technische Universität Braunschweig, Braunschweig, Germany

<sup>2</sup>Fraunhofer Institute for Surface Engineering and Thin Films, IST, Braunschweig, Germany

## Correspondence

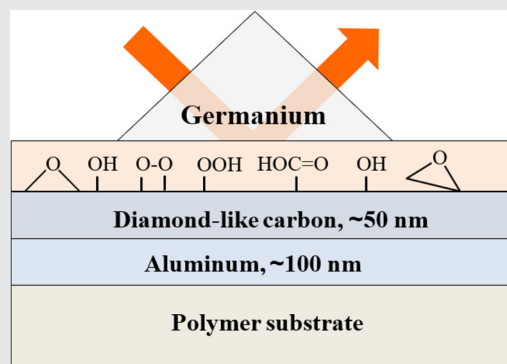
Claus-Peter Klages, Institute for Surface Technology, IOT, Technische Universität Braunschweig, Riedenkamp 2, 38108 Braunschweig, Germany.  
Email: [c-p.klages@tu-braunschweig.de](mailto:c-p.klages@tu-braunschweig.de)

## Funding information

Deutsche Forschungsgemeinschaft (DFG)

## Abstract

To study chemical functional groups on surfaces of diamond-like carbon (DLC) films, a highly sensitive infrared reflection-absorption spectroscopic technique, immersion infrared reflection-absorption spectroscopy (IRRAS), is applied in the present study. The method employs (i) a conventional attenuated total reflection (ATR) accessory with a Ge crystal as an immersion medium and (ii) an aluminum underlayer beneath the 50–70 nm thick DLC film. Sensitivity, selectivity, and quantifiability of the method can be enhanced by chemical derivatization (CD), coupling chemical moieties with strong characteristic vibrational bands to specific functional groups on the DLC surface. The method is applied to amorphous sputtered carbon films (a-C) to demonstrate that electrophilic groups, most probably epoxy groups, are formed during aging under ambient conditions.



## KEYWORDS

aging, derivatization, diamond-like carbon (DLC), infrared reflection-absorption spectroscopy (IRRAS), surface composition

This is an open access article under the terms of the Creative Commons Attribution-NonCommercial-NoDerivs License, which permits use and distribution in any medium, provided the original work is properly cited, the use is non-commercial and no modifications or adaptations are made.

© 2023 The Authors. *Plasma Processes and Polymers* published by Wiley-VCH GmbH.

# 1 | INTRODUCTION

## 1.1 | Motivation

Thin amorphous films consisting of highly crosslinked, hydrogen-free or hydrogenated networks of carbon atoms (a-C, a-C:H), also known as diamond-like carbon (DLC) films, are increasingly finding interest and applications as biomedical coatings, aside from other applications. DLC coatings combine favorable mechanical properties such as high hardness and wear resistance as well as low friction coefficients, with diffusion barrier properties, chemical resistance, and biocompatibility. Several review articles and monographies cover applications of DLC as body implants.<sup>[1–4]</sup>

For the interaction of a DLC-coated implant with animal cells in the presence of biological liquid, the formation of a protein layer on the biomaterial is generally decisive. The interaction with proteins, in turn, depends on physico-chemical properties like surface free energy and electro-kinetic (or zeta-) potential. Individual chemical surface moieties contribute to these properties collectively via dispersive, acid–base, and electrostatic double-layer interactions. Reactive functional surface groups, on the other hand, can result in more specific chemical interactions and bond formation. The covalent bonding of an extracellular matrix (ECM) protein such as tropoelastin or fibronectin (FN) may support the proliferation of endothelial cells, rendering a biomaterial hemocompatible, see, for example, Ganesan et al.<sup>[5]</sup> On the other hand, a mere adsorption of FN instead of covalent bonding may be

advantageous for certain applications because more bioactive RGD domains of the FN are maintained, resulting in better cell adhesion, as shown, for example, in Zhang et al.<sup>[6]</sup> For emerging orthodontic applications of DLC in the oral cavity, too, covalent protein bonding is undesirable because it may induce the formation of a biofilm.<sup>[7]</sup> Finally, reactive groups on the DLC surface may be used to immobilize bioactive biomolecules such as antithrombogenic heparin.<sup>[8]</sup> These examples may suffice to demonstrate that an understanding and control of chemical surface reactivity of DLC films is essential for their applications in advanced biomedical devices.

One purpose of this article is to test the hypothesis that the ability of DLC coatings to bind proteins covalently, reported, for example, in Ganesan et al.<sup>[5]</sup> and in other papers cited therein, is due to the presence of oxygen-containing functional groups with electrophilic reactivity on DLC surfaces. These groups are formed upon exposure to air.

In several previous studies of the chemical composition of DLC surfaces, X-ray photoelectron spectroscopy (XPS) was used as an analytical tool to gain information about the chemical nature of major oxygen-containing functional groups. Aside from — or in addition to — the frequently applied deconvolution of C1s spectra into four components with different numbers of bonds with oxygen, chemical-derivatization (CD) was often applied in combination with XPS (CD-XPS). This technique was already used in the early 80s for studies on plasma-treated polyethylene (PE) surfaces.<sup>[9–11]</sup> As to be seen in Table 1, giving an overview of selected papers in which XPS analysis was applied to

TABLE 1 Basic information from selected papers reporting XPS analyses of DLC films.

Film method	Analysis	Reagents/methodology	Ref. Year
a-C, Si:H PACVD	LP-CD & XPS	FOCS: Quantification of surface silanol groups, Si–OH	[12, 13] 2005, –2006
10 nm DLC proprietary	VP-CD & XPS	PFPH, TFAA, TFE for C=O, –OH, –C(=O)–OH, group densities increasing over about 2 weeks.	[14] 2007
a-C:H UBMS	XPS	4-component deconvolution of C1s band: Bulk sp <sup>2</sup> , surface sp <sup>2</sup> , bulk sp <sup>3</sup> , surface sp <sup>3</sup>	[15] 2008
a-C:H ID	VP-CD & XPS	HYD, TFAA, TFE for C=O, –OH, –C(=O)–OH	[16] 2010
a-C:H RF-PACVD	VP-CD & XPS	4-component deconvolution of C1s: C–C/C–H, C–O, C=O or O–C–O, O–C=O; CD: TFEH, TFAA for C=O, –OH	[17] 2011
a-C:H RF-PACVD	XPS	4-component deconvolution of C1s: C–C/C–H, C–O, C=O or O–C–O, O–C=O	[18] 2014
a-C:H ta-C	XPS	5-component deconvolution of C1s: C(sp <sup>2</sup> ), C(2p <sup>3</sup> ), C–O, C=O or O–C–O, O–C=O or O–(C=O)–O	[19] 2016

Abbreviations: DLC, diamond-like carbon; FOCS, tridecafluoro-1,1,2,2-tetrahydrooctyl-dimethylchlorosilane; HYD, hydrazine; ID, ionized deposition; PACVD, plasma-activated chemical vapor deposition; PFPH, pentafluorophenylhydrazine, RF-PACVD, radio-frequency PACVD; TFAA, trifluoroacetic anhydride; TFE, trifluoroethanol; TFEH, 2,2,2-trifluoroethylhydrazine; ta-C, tetrahedral amorphous carbon; UBMS, unbalanced magnetron sputtering; XPS, X-ray photoelectron spectroscopy.

DLC films, CD was mostly applied as a heterogeneous reaction (vapor-phase CD, VP-CD, or liquid-phase CD, LP-CD), using vapors or solutions of a reagent expected to react in a predictable way with functional groups on the DLC surface.

The XPS-based methodology applied in the cited papers is basically the same as it has frequently been used, for example, for the analysis of polymers, oxidized by plasma exposure, thermally, or upon aging in ambient air, as well as for plasma polymers. This approach is, however, not fully satisfying for the analysis of DLC films, consisting — in a somewhat simplified picture — of two kinds of “phases” A and B. In (A) carbon is present in the form of a highly crosslinked  $sp^3$ -bonded covalent network of C atoms with a varying content of H atoms, in (B) in extended clusters of  $sp^2$ -hybridized carbon atoms,<sup>[20,21]</sup> similar to more or less defective cutouts from graphene sheets. From a heuristic point of view it is useful and instructive to compare the  $sp^2$ -bonded part of aged, that is, oxidized DLC with other materials predominantly consisting of  $sp^2$  carbon. Such materials are, for example, partially oxidized soot, polycyclic aromatic hydrocarbons (PAHs), or carbon nanotubes (CNTs),<sup>[22,23]</sup> as well as sheets of graphene oxide (GO).

These substances carry diverse kinds of functional groups like hydroxyl, carbonyl, carboxyl, epoxy, lactone, anhydride, quinone, pyrone moieties, in addition to a large number of isolated or conjugated C=C double bonds, see, for example, Figures 1 and 2 in the recent review article about this material.<sup>[25]</sup> The abundance of diverse reactive functional groups and of unsaturated

C=C bonds opens pathways for chemical reactions which play no or only a minor role in modified polymers. Therefore, the methodology for CD-XPS analysis of DLC surfaces has to be adapted. For example, it has to be taken into account that trifluoroacetic anhydride (TFAA) can react not only with –OH groups but also with epoxides by ring opening<sup>[26,27]</sup> and with anhydrides by formation of mixed anhydrides.<sup>[28]</sup> For the derivatization with hydrazines,<sup>[9,29–31]</sup> too, it has to be taken into account that these reagents are generally not selectively indicating the presence of ketones and/or aldehydes by hydrazone formation but can also undergo reactions with carboxylic acids and aromatic esters<sup>[32,33]</sup> and even hydroxyls.<sup>[34]</sup> Coupling of hydrazines to carboxylic acids is most likely due to the formation of hydrazinium salts ( $R-NH-NH_3^+ R'-CO_2^-$ ).<sup>[35]</sup> On oxidized DLC surfaces, electrophilic cyclic oxygen functionalities such as epoxy, lactone, pyrone, and anhydride groups, as well as quinones, are potential hydrazine-reactive moieties. Last but not least, the presence of  $\alpha,\beta$ -unsaturated carbonyl- or carboxyl-containing groups enables reactions with nucleophilic derivatization reagents such as hydrazines and amines via (aza-)Michael addition to the activated double bond.<sup>[36]</sup>

To distinguish different kinds of bonding of a derivatization reagent, it is necessary to utilize alternative or additional analytical methods, beyond the

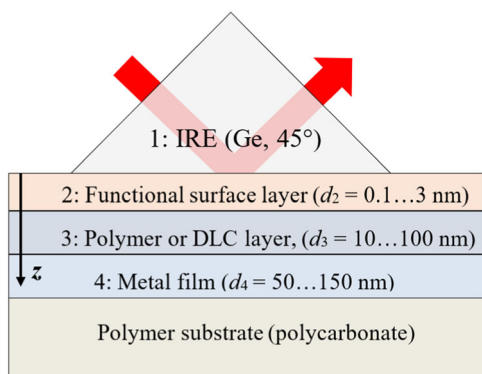


**FIGURE 1** Principle of immersion infrared reflection-absorption spectroscopy (IRRAS) (ImIRRAS) (not to scale): internal reflection element (IRE) in contact with a polymer or diamond-like carbon (DLC) film (gray) carrying an ultrathin surface layer with functional groups to be detected (orange). The metal film is deposited on a polycarbonate substrate with a very even surface, cut from a commercial compact disk, providing flexibility and good optical contact of IRE and DLC surface, thanks to an excellent surface quality and smoothness with typical roughness  $R_a < 6$  nm.<sup>[24]</sup>

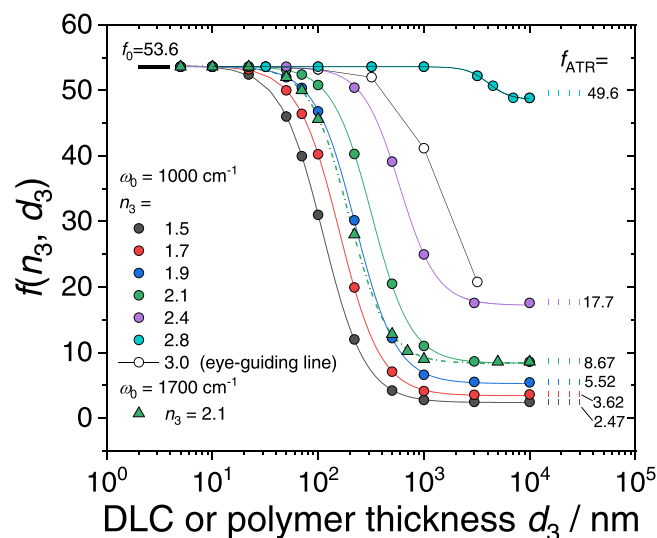


**FIGURE 2** Results of numerical optical calculations: Data points  $f$  as functions of layer thickness  $d_3$  for seven different refractive indices  $n_3$ ,  $2.1 < n_3 < 3.0$ . Colored curves are empirical fits with 4-parameter sigmoidal functions  $f_s$ , see Table 2 for function parameters. Values of  $f$  calculated with analytical formulas (see above) are shown as a compact black line for  $d_3 = 0$  ( $f_0 = 53.6$ ) and as dotted colored lines for  $d_3 \gg d_p$  ( $f_{ATR}$ ), for numerical values see the legend.

commonly used (CD)-XPS. For the chemical analysis of GO and other, related forms of carbon with a high degree of unsaturation such as soot<sup>[37]</sup> or different kinds of chars,<sup>[38]</sup> vibrational spectroscopy has been a valuable tool for studies of chemical functionality and reactivity. Therefore, the second purpose of the present article is to show that a special infrared-spectroscopic method, immersion infrared reflection absorption spectroscopy (ImIRRAS) can be applied to obtain qualitative and quantitative analytical information about the aged DLC surface with high sensitivity.

In the following section, the ImIRRAS method will be presented in more detail. After Section 2, the results of investigations on two batches of aging nominally hydrogen-free sputtered amorphous carbon coatings (a-C) will be presented and discussed.

## 1.2 | Immersion infrared reflection-absorption spectroscopy (ImIRRAS)

To make IR-spectroscopic information about the DLC surface chemistry more easily accessible, use was made of a special version of the infrared reflection-absorption (IRRAS) method. For this purpose, an internal reflection element (IRE) with a high refractive index and a highly reflective metal film at a distance of 10–100 nm from the DLC surface are employed, as illustrated in Figure 1. Here, the ultrathin “functional surface layer” represents the surface region of the DLC film in which the functional groups of interest are residing.

The measurements can be done with the conventional attenuated total reflection (ATR) accessory of an IR spectrometer. Although this will not necessarily provide the optimum conditions in terms of the angle of incidence and refractive index of the IRE,<sup>[39]</sup> substantial sensitivity enhancements can be achieved, compared with ATR, as will be shown below. The ImIRRAS method differs from ATR by the presence of the metal layer within reach of the evanescent wave coupled into the layer system by the IRE element: With the absorbing metal layer, total reflection is no longer possible. On the other hand, the method differs from the conventional IRRAS method by the presence of the IRE, serving as an immersion medium.

To obtain quantitative information about the densities of functional groups with high selectivity and sensitivity, chemical derivatization can be applied to tag the surface with strong infrared absorbers. In the present paper, reagents with  $-CF_3$  groups are employed, resulting in strong IR absorptions in the wavenumber region between 1100 and 1300  $cm^{-1}$ , due to the symmetric and asymmetric vibrations of the trifluoromethyl group. The

absorptions measured on derivatized DLC surfaces are compared with absorptions due to comparable vibrations in solutions of selected model compounds with known concentrations, presuming that these model compounds have the same oscillator strengths as the tags on the DLC surface.

The applied evaluation procedure makes use of Harrick's concepts of effective thickness,  $d_e$ ,<sup>[40]</sup> and of integrated intensities,  $B$ ,<sup>[41]</sup> of model compounds. To calculate functional group densities,  $\rho$ , from areas of characteristic bands in the absorbance spectra measured by ImIRRAS, Equation (3) is used. Therein  $\bar{\nu}$  is the wavenumber,  $B$  the wavenumber-integrated molar absorption coefficient,  $\epsilon$ , (“integrated intensity”),  $f$  the ratio of the effective thickness,  $d_e$ , and the physical thickness of the functional surface layer,  $d_2$  (#2 in Figure 1). Equation (3) follows from the integrated Beer–Lambert law, Equation (1):  $d_e$  is the thickness which a fictitious thin layer with constant molar absorber concentration  $c$  would have to have to obtain, in a transmission measurement, the same absorbance as in the ImIRRAS spectrum.<sup>[40]</sup> In Equation (2), implicitly defining  $f$  and  $B$ , the areal molar density,  $\rho$ , is written for the product  $c \times d_2$ . In fact, the measured ImIRRAS spectrum is independent on the actual distribution of the absorber along the coordinate  $z$  (see Figure 1) within an ultrathin surface region, it depends only on the integral of  $c(z)$  over  $z$  which is the more general definition of  $\rho$ .

$$\int A(\bar{\nu}) d\bar{\nu} \equiv \int \log(R_p^{-1}(\bar{\nu})) d\bar{\nu} = c d_e \int \epsilon(\bar{\nu}) d\bar{\nu}, \quad (1)$$

$$c d_e \int \epsilon(\bar{\nu}) d\bar{\nu} \equiv c d_2 f \int \epsilon(\bar{\nu}) d\bar{\nu} \equiv \rho f B, \quad (2)$$

$$\rho = \frac{1}{f B} \int A(\bar{\nu}) d\bar{\nu}; \quad \rho_n \equiv \rho N_A. \quad (3)$$

In Equation (3),  $\rho_n$  is the areal number density of absorbers. The factor  $f \equiv d_e/d_2$  depends on the polarization and angle of incidence,  $\theta$ , of the IR beam, refractive indices  $n$  of media #1 to 4 and the absorption index of the metal layer,  $k_4$ . The layer #3 is considered virtually free of IR absorbers in the wavenumber region of interest,  $k_3 = 0$ . For the limiting case of ATR, where the thickness  $d_3$  is well beyond the penetration depth,  $d_p$ , of the evanescent wave,  $d_3 \gg d_p$ ,  $f_{ATR}$  can be calculated by analytical formulas given by Harrick and Carlson (eqs. (5a) and (5b) in Harrick et al.<sup>[40]</sup>). For the case of  $d_3 = 0$ , on the other hand, equations derived by McIntyre and Aspnes are available for the small thickness of layer #2,

$d_2 < 10^{-3}/\bar{\nu}^{[42]}$ ; a practical approximation was reported by Chabal, see eq. (2.19) of Chabal<sup>[43]</sup> Slightly adapted to the present study this equation, valid for angles  $\theta$  below  $85^\circ$ , reads:

$$\left[ \frac{\Delta R}{R} \right]_p \cong 8 \pi \bar{\nu} n_1^3 d_2 \frac{\sin^2(\theta)}{\cos(\theta)} \text{Im} \left( \frac{-1}{\epsilon^*_2} \right). \quad (4)$$

$\epsilon^*_2$  is the permittivity of medium 2. From this equation and the corresponding expression for normal transmission through the film,  $(\Delta T/T)_\perp = 2 \pi \bar{\nu} \text{Im}(\epsilon^*_2) d_2/n_2$ ,<sup>[39]</sup>  $f_0 = 53.6$  is calculated by numerical integration with *MATLAB* and division of the integrals. The extension to multiple surface layers by McIntyre<sup>[44]</sup> cannot be used in the present study because  $d_3$  is generally too large, typically between 10 and 100 nm. Therefore, numerical optical calculations were used to obtain  $f$  for the parameter range of interest in the present context, using the *SpectraRay/4* software package (SENTECH Instruments GmbH).

Corresponding with the experiments reported below,  $n_1 = 4$  and  $\alpha = 45^\circ$  were used for an IRE from germanium;  $k_3 = 0$  and  $n_3 = 1.5, 1.7, 1.9, 2.1, 2.4, 2.8,$  and  $3.0$  respectively, were chosen for the interlayer #3, to represent the range of refractive indices typical of polymer-like films on the one hand and high-density DLC on the other. For an oscillator layer close to the metal layer, only parallel polarization is useful.<sup>[39]</sup> As a metal layer aluminum was chosen, with optical parameters from Ordal et al.<sup>[45]</sup> To obtain  $f$ , a 1-nm-thick model layer with a single Lorentz oscillator layer<sup>[39]</sup> was defined as layer #2 to calculate the band areas resulting with ImIRRAS on the one hand and in normal transmission through the layer, arranged between two semi-infinite media with refractive indices of  $n = 1.5$ , on the other. For most calculations, oscillator parameters (applying the conventional nomenclature, with symbols  $\omega$  for wavenumber and  $\epsilon_\infty$  for the real part of  $\epsilon^*$  at high frequency) were:  $\epsilon_\infty = 2.25$ ,  $\omega_0 = 1000 \text{ cm}^{-1}$ ,  $\omega_p = 100 \text{ cm}^{-1}$ , and  $\gamma = 10 \text{ cm}^{-1}$ . Results are shown in Figure 2.

Parameters used for the empirical fit to the data points with  $1.5 < n_3 < 2.8$  in Figure 2 are collected in Table 2. As  $n_3$  reaches 2.83, the critical angle of total reflection,  $\sin^{-1}(2.83/4)$ , becomes  $45^\circ$ , and ATR with Ge is no longer possible at  $45^\circ$  angle of incidence. However, with  $d_3 = 300 \text{ nm}$ , as an example,  $f \approx 52$  can still be achieved, see empty data points in Figure 2. Please note the reasonable agreement of  $A_1$  and  $A_2$  values in Table 2 with figures  $f_0$  and  $f_{\text{ATR}}$  in Figure 2, obtained by analytical formulas for the limiting cases of  $d_3 = 0$  and  $\infty$ , respectively.

TABLE 2 Parameters of the sigmoidal functions  $f_s$  used for fits in Figure 2.

	$f_s(d_3) = A_2 + (A_1 - A_2)/(1 + (d_3/d_{3,0})^p)$						
$n_3$	1.5	1.7	1.9	2.1	2.4	2.8	2.1 <sup>a</sup>
$A_1$	53.8	53.7	53.7	53.7	53.6	53.6	53.7 <sup>a</sup>
$A_2$	2.39	3.43	5.27	8.38	17.2	48.6	8.36 <sup>a</sup>
$d_{3,0}$	111	158	225	321	589	4074	195 <sup>a</sup>
$p$	2.16	2.19	2.24	2.33	2.46	4.24	2.36 <sup>a</sup>

<sup>a</sup>Parameters in this column were calculated with  $\omega_0 = 1700 \text{ cm}^{-1}$ , all else with:  $\omega_0 = 1000 \text{ cm}^{-1}$

To obtain a large  $f$ , an angle of  $45^\circ$  is generally not the optimum: For the case of immersion IRRAS without an interlayer ( $d_3 = 0$ ), optimum conditions were discussed in detail by Tolstoy et al.<sup>[39]</sup> In the present case  $f_0(60^\circ) = 109$  and  $f_0(81^\circ) = 304$  should be achievable, all else unchanged. For the ATR limit, on the other hand, lower angles are preferable, for example,  $f_{\text{ATR}}(n_3 = 1.5, \theta = 35^\circ) = 3.15$ .

The choice of  $\omega_0 = 1000 \text{ cm}^{-1}$  was motivated by the fact that many diagnostically relevant vibrations such as  $\text{CF}_3$  stretching vibrations or deformation vibrations of the epoxy ring are located in the wavenumber region between 700 and  $1300 \text{ cm}^{-1}$ . For  $\omega_0 = 1700 \text{ cm}^{-1}$  as the typical wavenumber of  $\text{C=O}$  stretching vibrations, the substantially shorter penetration depth of the IR radiation results in a shift of the sigmoidal curves, as shown exemplarily for  $n_3 = 2.1$  in Figure 2 (triangles) and the corresponding fit parameters in Table 2.  $A_1$  and  $A_2$  are virtually independent from the wavenumber.

It must be noted, however, that the choice of  $\epsilon_\infty$  for the oscillator layer has a relatively large influence on the results. A value of  $\epsilon_\infty = 2.25$ , corresponding to a refractive index of  $n_2 = 1.5$ , was chosen here, led by the hypothesis, that the upper ultrathin surface layer has polymer-like properties; polymers frequently have refractive indices close to 1.5.<sup>[46]</sup> Choosing  $n_2 = 1.6$  instead, that is,  $\epsilon_\infty = 2.56$ , would decrease  $f_0(\omega_0 = 1000 \text{ cm}^{-1})$  from 53.6 to 44.2, that is, by 18%. In the ATR limit,  $f_{\text{ATR}}(n_2 = 1.6, n_3 = 1.5) = 2.28$  (−5%) and  $f_{\text{ATR}}(n_2 = 1.6, n_3 = 2.1) = 7.37$  (−12%), all else unchanged. The uncertainty concerning the choice of  $\epsilon_\infty$  is therefore probably the most important source of systematic error.

It is evident from Figure 2 that the ImIRRAS method is especially useful for (sputtered) amorphous carbon coatings for which the refractive index for photon energies near 0.1 eV is generally beyond 2.1.<sup>[47,48]</sup> Therefore, for a-C films with thicknesses up to 70 nm as in the present study,  $f$  will still be larger than 50.

## 2 | EXPERIMENTAL

### 2.1 | Materials

4,4,4-Trifluorobutylamine (TFBA) was obtained from Apollo Scientific, 2,2,2-trifluoroethylhydrazine (TFEH) from Sigma Aldrich (70% solution in water), tetrachloroethylene (ultra-pure, spectrophotometric grade) from Thermo Scientific (Germany). All reagents were used as received.

### 2.2 | Procedures

#### 2.2.1 | Deposition of aluminum and DLC

Aluminum films, typically 100 nm thick, and nominally hydrogen-free amorphous carbon films (a-C), typically 50–60 nm thick, were deposited consecutively, without intervening venting, by direct current (DC) magnetron sputtering in an *Inline Coater SV470* (FHR Anlagenbau GmbH, Ottendorf-Okrilla). Polycarbonate (PC) substrates of  $1.5 \times 1.5 \text{ cm}^2$  size were cut from commercial compact disks (CDs), cleaned by 30-min sonication in isopropanol and mounted on the substrate holder using double-sided tape. For sputtering, argon with 5.0 purity was applied. Electrical sputter parameters and Ar pressures were: Al target (99.999% pure,  $25.4 \times 12.7 \text{ cm}^2$ ): 385 V, 2.6 A (1 kW), 1.0 Pa. Graphite target (99.99% pure,  $47.0 \times 13.0 \text{ cm}^2$ ): 480 V, 2.1 A (1 kW), 0.1 Pa. Two batches of samples were coated under nominally identical conditions, in the following called batches B1 and B2.

The samples were stored under ambient laboratory conditions ( $21 \pm 1^\circ\text{C}$ ,  $40 \pm 10\%$  rel. humidity) in covered Petri dishes made from glass.

#### 2.2.2 | Chemical derivatization

Vapor-phase derivatization reactions were carried out in *In-Ex-Tubes 29T* from FengTecEx GmbH with the samples placed in the inner tube and about 200  $\mu\text{L}$  of liquid reagent at the bottom of the outer tube. After closing the tube, the reagent (TFBA) was cooled by dipping the tube end into liquid nitrogen and the tube was evacuated by a rotary vane pump. Samples were left in the tube at room temperature overnight and, on the next day, transferred to into a heatable desiccator which was evacuated at  $40^\circ\text{C}$  for 2 h with continuous pumping to remove physisorbed reagent.

For liquid derivatization, the samples were placed in deaerated aqueous solutions of the reagent for a specified duration and were subsequently thoroughly rinsed with deionized water to remove physisorbed reagent.

### 2.3 | Characterization and analysis

#### 2.3.1 | Ellipsometry

Ellipsometric measurements of thickness and refractive index of a-C thin films were made using a spectroscopic ellipsometer (*SE 850 DUV*, Sentech Instruments GmbH) at incident angles from  $50^\circ$  to  $70^\circ$  with  $5^\circ$  increments in the wavelength range of 380–900 nm. Thicknesses were calculated using the SpectraRay/4 software package (Sentech) with a Tauc-Lorentz model for the carbon layer. Results for batches B1 and B2 are:  $d_{B1} = 65 \pm 1 \text{ nm}$  and  $d_{B2} = 68 \pm 1 \text{ nm}$ ,  $n(589 \text{ nm}) = 2.13 \pm 0.05$ .

#### 2.3.2 | Fourier transform infrared (FTIR) spectroscopy

For infrared spectroscopy, an FTIR spectrometer *Nicolet iS50* (Thermo Fisher Scientific GmbH) was used, equipped with a mercury cadmium telluride and a deuterated triglycine sulfate detector. For the ImIRRAS studies an ATR accessory Smart iTX was used with a single reflection Ge crystal. Transmission measurements on solutions of CD reagents TFBA and TFEH in tetrachloroethylene were performed in a cuvette equipped with NaCl windows and a lead gasket providing a path length of  $140 \pm 3 \mu\text{m}$  as determined from the interference pattern in an empty-cell spectrum. FTIR measurements were usually done in the wavenumber range of  $4000\text{--}650 \text{ cm}^{-1}$  with a spectral resolution of  $4 \text{ cm}^{-1}$ , averaging 64 scans.

#### 2.3.3 | X-ray photoelectron spectroscopy (XPS)

For XPS a *PHI 5500 ESCA* system (Physical Electronics) was used, equipped with a hemispherical analyzer and a Mg  $K\alpha$  X-ray source (1253.6 eV). The angle between X-ray source and the analyzer was  $54.7^\circ$ . High-resolution spectra were acquired at a constant analyzer pass energy of 11.75 eV and an electron take-off angle of  $47^\circ$  with respect to the sample surface. *PHI MultiPak* instrument software was used to evaluate the spectra.

### 3 | RESULTS AND DISCUSSION

#### 3.1 | Oxygen uptake measurement by XPS

Results of XPS measurements on surfaces of a-C samples from batch B1, aged up to 21 days under the above-given conditions, are displayed in Figure 3. The C1s peak in the XPS spectrum measured on day 21 was deconvoluted into six components. Table 3 shows binding energies  $BE_i$  and mole fractions  $x_i$  for individual components  $i$  as obtained from the best fit.

The deconvolution of C1s peaks in XPS spectra of carbonaceous compounds has been the subject of research until recently.<sup>[49–54]</sup> A reliable analysis requires to know the fractions of  $sp^2$ - and  $sp^3$ -bonded carbon atoms as well as their fitting parameters. As this information was not available for the present samples, several curve fittings were executed with different assumptions regarding graphitic carbon ( $sp^2$ , C=C) and aliphatic carbon ( $sp^3$ , C–C, C–H), to investigate the influence on peak areas of components representing C atoms bound to oxygen. Curve fitting was done with six components whereof three represent oxygen-bound carbon. The same full width at half-maximum (FWHM = 1.8 eV) was used for the latter components, and also for the aliphatic carbon peak. For graphitic C, an asymmetric curve shape was applied, with a maximum restricted to the range of 284.3–284.6 eV. The peak difference between aliphatic and graphitic carbon ( $BE_2 - BE_1$ ) was restricted to the range of 0.3–0.5 eV. The satellite peak difference relative to the graphitic carbon peak was fixed to 6.4 eV. Data shown in Table 3 are obtained in the best fit among a range of fits executed with varying parameters. It must be noted that minor changes in parameters used for components 1 and 2 result in large variations of the molar fractions of oxygen-bonded carbon, typically within a range of  $\pm 10\%$ . In spite of the relatively large error of  $x_3$  it appears that among O-bonded C atoms those with a single bond to O dominate with about 60%. Comparing the results in Table 3 with the oxygen mole fraction of 8.6% (Figure 3), one is led to conclude that for component 3 C–O–C bonds are probably dominating, for component 4 C=O bonds. The first assumption is substantiated by results obtained with infrared spectroscopy, pointing to an appreciable amount of epoxy groups formed in the first hours of aging, see Section 3.2. However, it must be pointed out that even under the assumption that oxygen is only contained in epoxy, carbonyl, and lactone groups, the oxygen content from the C1s analysis would be  $(x_3 - x_5)/2 + x_4 + 2x_5 = 10.5\%$ , versus 8.6% from the O1s/C1s area ratio. Similar and even larger overestimations of

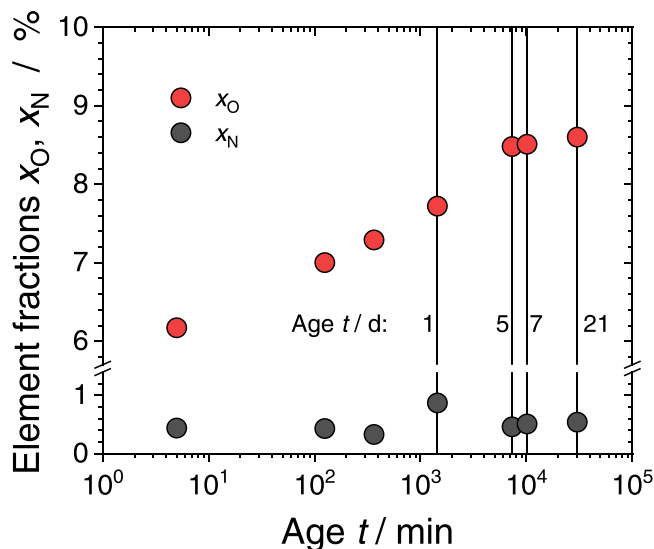


FIGURE 3 Evolution of oxygen and nitrogen mole fractions on the surfaces of a-C films during aging up to 21 days (B1).

TABLE 3 C1s peak deconvolution for a sample from batch B1 at  $t = 21$  d.

$i$	$BE_i$ /eV	$x_i$ /%	Possible binding
1	284.4	21.4	C=C ( $sp^2$ )
2	284.7	54.4	C–C, C–H ( $sp^3$ )
1&2		75.8	(Sum of 1 and 2)
3	286.5	8.6	C–O–C, C–OH
4	288.2	3.9	C=O, O–C–O
5	289.3	1.5	O–C=O
6	290.8	1.0	$\pi$ - $\pi^*$ satellite of C=C

Note: Best fit results.

oxygen by the “conventional” C1s deconvolution have in the past frequently been reported for XPS analyses of graphitic or graphene-based materials with extended  $sp^2$ -hybridized domains, see the citations in the paper by Kovtun et al.<sup>[50]</sup> With advanced deconvolution methods, this discrepancy can be reduced or removed as shown in recent publications but this research topic is outside the scope of the present work.

The time dependence of  $x_O$  displayed in Figure 2 up to 21 days is similar to findings by Kondo and Nishida<sup>[14]</sup> in VP-CD-XPS studies on a-C:H. In those investigations, however, the increase of  $x_O$  between day 0 and day 6 was mainly due to C=O groups, accounting for 54% of O-functional groups (OH, C=O, COOH) on day 20. In the present case about 60% of functional groups on 21-day-old a-C had a single C–O bond and only between 22% and 27% two bonds to O (C=O, O–C–O). Cloutier et al., on the other hand, applying C1s deconvolution for the analysis

of a-C:H directly after deposition and after 3 years, respectively, reported that the aging process predominantly generated C–O bonds.<sup>[18]</sup> Both papers are in conflict with results reported by a Japanese group<sup>[16]</sup> based on VP-CD-XPS according to which C=O groups are already predominant in freshly prepared a-C:H.

Different results that can be found in the literature for the surface composition of a-C:H may be due to different deposition and storage conditions. It cannot be excluded, however, that discrepancies are also caused by the failure of “traditional” assumptions made for the selectivity of chemical derivatization reactions.

### 3.2 | Aging of DLC as measured by ImIRRAS

Spectra shown in Figure 4 were taken one after the other over 150 min during aging of a batch of 10 a-C samples from one deposition run (B2), starting with a first measurement 10 min after opening the unloading compartment of the sputter apparatus. The following discussion will be organized according to the regions R1 through R4, highlighted in color in Figure 4.

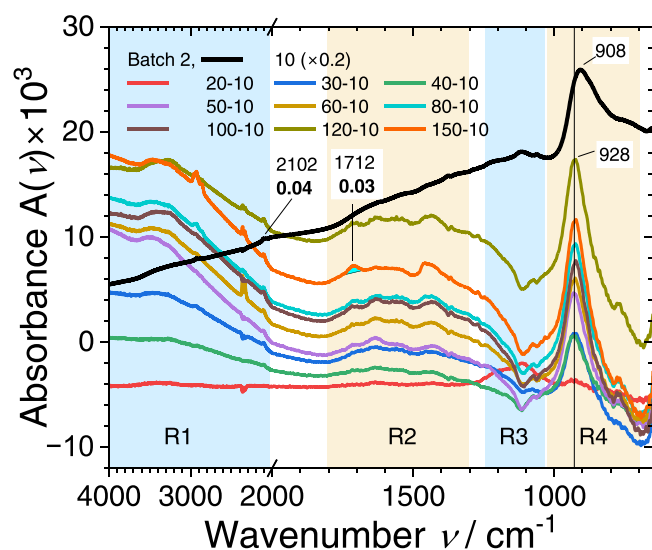


**FIGURE 4** (left) ImIRRAS spectra of a-C films from B2 with ages between 10 and 150 min. The spectrum with label “10 ( $\times 0.2$ )” is from a 10-min old sample, scaled by a factor of 0.2. Labels “ $i$ -10,” and so on, denote difference spectra: The original 10-min spectrum is subtracted from spectra of samples  $i$  minutes old. The carbonyl band at  $1712\text{ cm}^{-1}$  is virtually absent at  $t = 10$  min but develops over 150 min when it finally attains a band area of  $0.03\text{ cm}^{-1}$ . The ketene band at  $2102\text{ cm}^{-1}$  has already an area of  $0.04\text{ cm}^{-1}$  in the 10-min spectrum; it increases to  $0.06\text{ cm}^{-1}$  within 150 min. The feature at  $2360\text{ cm}^{-1}$  is due to  $\text{CO}_2$  in the beam path. Note that there is a significant difference in positions of peaks at  $908\text{ cm}^{-1}$  in the 10-min spectrum and at  $928\text{ cm}^{-1}$  in the difference spectra.

The series of 10 spectra shown in Figure 5 helps to understand the occurrence of inverted peaks in region R3 of Figure 4: These 10 spectra were offset vertically to coincide at  $1400\text{ cm}^{-1}$ . This presentation shows that there is, already in the first spectrum, a band with a peak at  $1113\text{ cm}^{-1}$ , somewhat increased at  $t = 20$  min and then decaying to virtually zero absorbance within about 100 min. Similar behavior can be seen for the peak at  $690\text{ cm}^{-1}$ . The difference spectrum “20–150” isolates these two bands from the background.

There is reason to presume that these transient bands are due to labile (hydro)peroxy groups formed upon contact of the freshly prepared a-C film surface with the open air. These groups could be formed in reactions between carbon-centered radicals with atmospheric oxygen and subsequent abstraction of hydrogen atoms from the film surface by the intermediately formed peroxy radicals. This mechanism is well known from oxidative degradation of polymers initiated by radical formation.<sup>[55]</sup> Although the films were sputtered using high-purity Ar and graphite, respectively, the presence of a substantial fraction of hydrogen cannot be excluded, originating, for example, from the residual gas or from the walls.<sup>[56,57]</sup> At least the  $1113\text{-cm}^{-1}$  peak falls well into the range of C–O vibrations in hydroperoxides.<sup>[58]</sup> A definite assignment, however, would require further studies.

It is important to note that at a film age of  $t = 10$  min the band below  $1000\text{ cm}^{-1}$  in region R4 of Figure 4 is largely due to an ultrathin oxide layer on the aluminum sublayer, beneath the a-C film. The further growth of this band, however, as seen in the difference spectra in

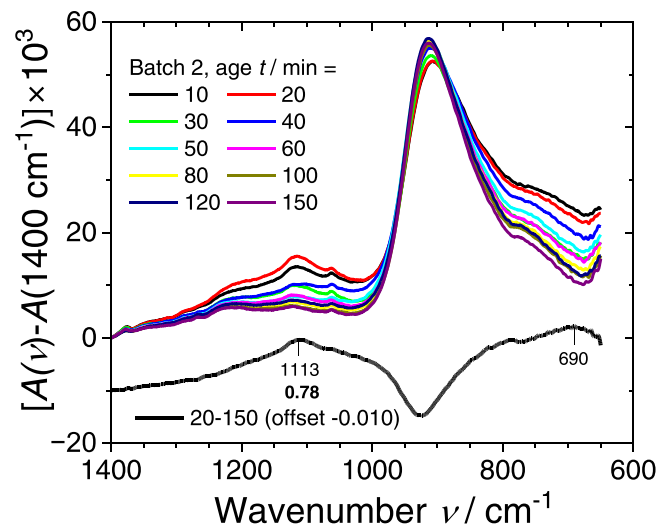


**FIGURE 5** (right) ImIRRAS spectra of a-C films (B2) with ages between 10 and 150 min, region of C–O and Al–O stretching vibrations between  $1400$  and  $650\text{ cm}^{-1}$ .



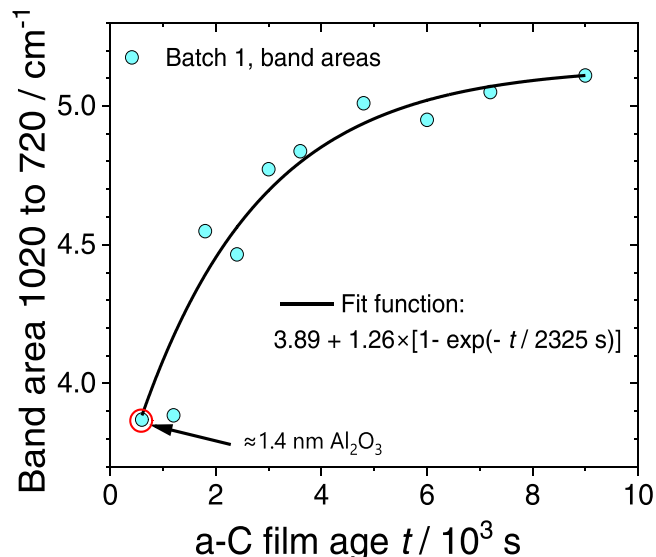


**FIGURE 6** (left) Growth of the area of the band with a peak between 908 and 924  $\text{cm}^{-1}$ , integrated from 1020 to 750  $\text{cm}^{-1}$ . Data points were fitted by the function given in the legend, approaching the value of 5.15  $\text{cm}^{-1}$  exponentially with a time constant of 2300 s (38 min).

Figure 4 as well as in the graph in Figure 6, showing the increase of band area between 1020 and 720  $\text{cm}^{-1}$  with time, is not due to further oxidation of the buried  $\text{Al}_2\text{O}_3$  layer upon exposure of the sample to air, but to the formation of functional groups on the a-C surface.

There are several arguments which can be put forward to underpin this important conclusion: There is (i) a substantial difference in peak positions at  $t=10$  min (908  $\text{cm}^{-1}$ ) and in the difference spectra (928  $\text{cm}^{-1}$ ) as well as (ii) in the FWHMs: 80  $\text{cm}^{-1}$  for the oxide which is mainly present at 10 min versus 120  $\text{cm}^{-1}$  for the difference spectra. (iii) The growth curve in Figure 6 does not have the typical shape of low-temperature oxide growth curves<sup>[60]</sup> and it is not plausible that the oxide growth stops after the thickness has increased from 1.4 nm to about 1.8 nm. Most important, however, are (iv) the changes in IR spectra upon exposing the DLC films to vapors or solutions of nitrogen nucleophilic amines and hydrazine, see Section 3.3.

The  $\text{Al}_2\text{O}_3$  thickness value given in Figure 6 was estimated, based on an optical simulation of a layer system, consisting of 2 nm  $\text{Al}_2\text{O}_3$  (Brendel oscillator<sup>[61]</sup>) on Al (Drude model<sup>[45]</sup>). Comparing a simulated spectrum of  $\log(1/R_p)$  obtained by IRRAS (80°) with an ImIRRAS spectrum (Ge 45°, 50 nm DLC with  $n=2.1$  and  $k=0$ ) resulted in a band area by a factor 7.3 larger for the ImIRRAS spectrum, in reasonable agreement with the ratio (see Equation [3])  $4^3 \sin(45^\circ) \tan(45^\circ) / [\sin(80^\circ) \tan(80^\circ)] = 8.10$ . For 80°-IRRAS measurements, a relation between band area

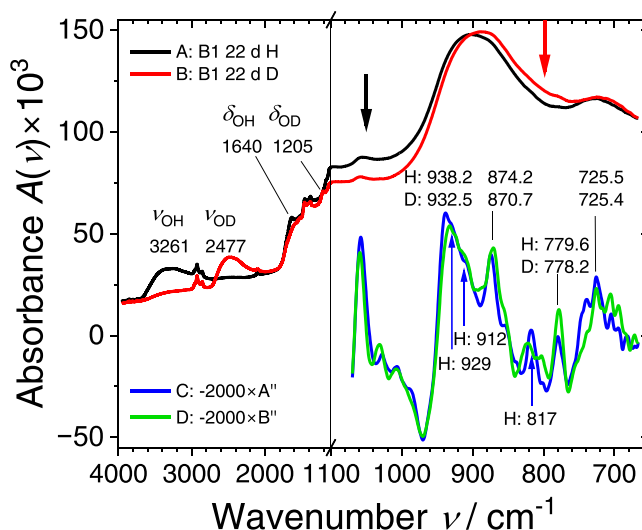


**FIGURE 7** (right) A, B: Averages of spectra from two 22-day old samples from B2, measured after 15 min exposure to vapors of  $\text{H}_2\text{O}$  (“H”, black) and  $\text{D}_2\text{O}$  (“D”, red), respectively, in air (about 45% relative humidity). Note the change of wavenumber scale at 1100  $\text{cm}^{-1}$ . Aside from vanishing or appearance, respectively, of stretching and deformation vibrational bands related to hydroxyl groups and adsorbed water ( $\nu_{\text{OH(D)}}$  and  $\delta_{\text{OH(D)}}$ ), there are major changes in the region below 1100  $\text{cm}^{-1}$ : Black and red arrows indicate the regions of maximum absorbance decrease and increase, respectively, upon exchange of H against D. Second derivatives of A and B, respectively, in graphs C and D (here multiplied by  $-2000$ , blue and green) reveal four major peaks in this region, with wavenumbers as indicated in the legend.<sup>[59]</sup> Wavenumber ratios of peak positions in H and D spectra are, from left to right: 1.006, 1.004, 1.002, and 1.000. A further peak and two shoulders in the H spectrum are marked by blue arrows.

and oxide thickness was established before.<sup>[60]</sup> With this information,  $d_{\text{ox}}(10 \text{ min}) = 1.4 \text{ nm}$  was estimated.

The wavenumber region below 1100  $\text{cm}^{-1}$  was studied in more detail on two 22-days old samples from batch B2, applying H/D isotope exchange of O-bonded hydrogen atoms. The second derivative of the average spectra of samples exposed 15 min to  $\text{H}_2\text{O}$  vapor and to  $\text{D}_2\text{O}$  vapor, respectively, with a relative humidity of 45% each, was inspected. Results are shown in Figure 7 in which A and B are spectra measured after exposure to  $\text{H}_2\text{O}$  and  $\text{D}_2\text{O}$ , respectively, while C and D are second derivatives of A and B, respectively, multiplied by  $-2000$ . The latter spectra show that the broad bands with peaks near 900  $\text{cm}^{-1}$  in A and B consist of at least two components with small effects of H/D exchange as shown by the peak positions given beyond the graphs. However, the shoulders of the band with a peak at 938  $\text{cm}^{-1}$  (H form) and the peak at 817  $\text{cm}^{-1}$  suggest that there are even more components, see the arrows and figures below the graphs.

In the context of the main motivation of the present study, it is important to note that the peaks between 1000 and 800  $\text{cm}^{-1}$  fall into the regions of antisymmetric and symmetric in-plane deformation vibrations, respectively, of epoxy rings.<sup>[62]</sup> These vibrations extend generally from (rounded) 950 to 860  $\text{cm}^{-1}$  and from 870 to 785  $\text{cm}^{-1}$ , respectively.<sup>[63]</sup> An epoxy ring “breathing” vibration, typically appearing between 1235 and 1280  $\text{cm}^{-1}$ , is not visible in the spectra. In spectra of model epoxides reported in the literature, too, the corresponding band has often less intensity than the ring deformation bands, see, for example, data in Bomstein<sup>[64]</sup> It is therefore assumed that the broad band in region R4 of Figure 4 can be assigned to epoxy groups in different bonding situations.

Arrows in black at 1050  $\text{cm}^{-1}$  and in red at 800  $\text{cm}^{-1}$  in Figure 7 mark the centers of relatively broad wavenumber regions where major changes in absorbance are to be seen as a result of H/D exchange. The large wavenumber shift indicates that C–O–H(D) deformation vibrations are involved here. A comparison with literature data for spectra of carboxylic acids, alcohols, and phenols shows that this region is not typical for in-plane or out-of-plane deformation vibrations of C–O–H groups in these classes of compounds.<sup>[58]</sup>

As shown in Figure 8, the total area of absorbance bands due to O–H stretching vibrations, appearing in region R1 of Figure 4, grows in the first 50 min to a value staying virtually constant over the following 100 min. Evidently, the band could be decomposed into at least two components with age-dependent weights. The C–H vibrations in this figure are most probably due to adventitious hydrocarbon contaminations. While both, the density of OH groups as well as that of presumed epoxy groups, virtually approaches a constant value within the first 50–100 min, the growth of the carbonyl group density proceeds much more slowly. The corresponding absorption band emerges at 1712  $\text{cm}^{-1}$ , see region R2 of Figure 4, and attains a band area of only 0.03  $\text{cm}^{-1}$  within the first 150 min. Figure 9 shows spectra taken at sample ages  $t = 150$  min, 1 day, and 18 days, respectively. Three- or four-digit numbers in these and the following figures are peak positions, bold figures are areas of absorption bands. After about 24 h, the carbonyl band has shifted to below 1700  $\text{cm}^{-1}$  and grown in area by 0.14  $\text{cm}^{-1}$ , see the red difference spectrum “(B–A)  $\times 10$ ”, and at  $t = 18$  days, the spectrum in the C=O-stretching region has changed further by additional intensity around 1650  $\text{cm}^{-1}$ . To estimate an order of magnitude of carbonyl group densities at day 1, using a value of 10,000  $\text{Lcm}^{-2}\text{mol}^{-1}$  as typical integrated intensity of a carbonyl groups<sup>[41]</sup> one arrives at a value of 2  $\text{nm}^{-2}$  while it is only 0.3  $\text{nm}^{-2}$  after 150 min, when the

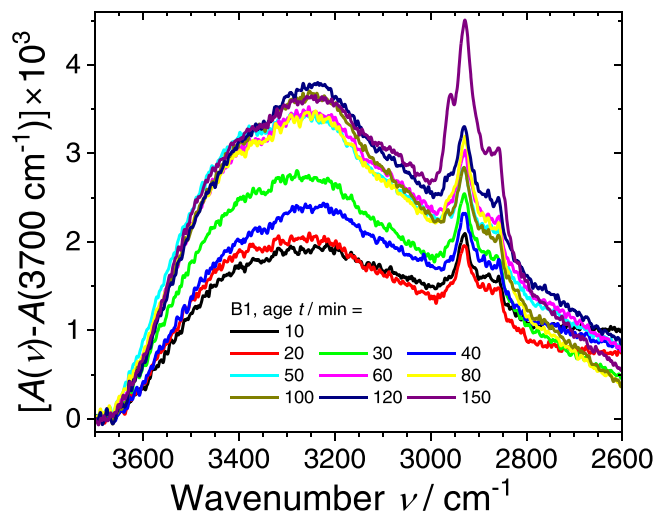


FIGURE 8 (left) ImIRRAS spectra of a-C films with ages between 10 and 150 min, region of O–H and C–H stretching vibrations between 3700 and 2600  $\text{cm}^{-1}$ . A linear background between data points at 4000 and 2400  $\text{cm}^{-1}$  was subtracted and the spectra were offset to coincide at 3700  $\text{cm}^{-1}$ .

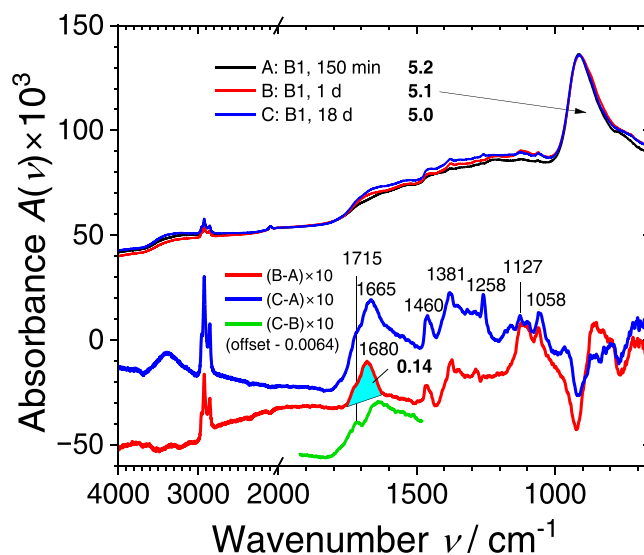


FIGURE 9 (right) Spectra taken after 150 min, 1 day, and 18 days, respectively. Difference spectra show effects of aging from 150 min to 1 day and 18 days, respectively, and from 1 day to 18 days. Note the shift in peak position of the C=O stretching vibration in the difference spectrum B–A to lower than 1700  $\text{cm}^{-1}$ . After 18 days, a peak at 1665  $\text{cm}^{-1}$  and a shoulder at 1715  $\text{cm}^{-1}$  are visible.

presumed epoxy band has already grown into saturation. Note that this band has an area of about 1.3  $\text{cm}^{-1}$ , an order of magnitude larger than the carbonyl band. This leads to the conclusion that the corresponding group density should be at least an order of magnitude larger than the carbonyl-group density because C–O stretching vibrations generally do not have larger integrated

intensities than C=O vibration which are usually very strong. In view of the oxygen mole fraction of roughly 0.1 as determined by XPS one can conclude that the oxidized layer must have a substantial depth, about 5 nm if a density of  $1\text{ g/cm}^3$  is assumed, to be consistent with  $\rho_n = 20\text{ nm}^{-2}$ . Preliminary angle-resolved XPS measurement support this conclusion.

### 3.3 | Reaction of aged a-C samples with TFBA and TFEH

Figures 10 and 11 display the results of chemical derivatization experiments performed on samples from batches B1 and B2. Figure 10 shows the result of liquid-phase experiments (LP-CD) with TFBA, Figure 11 results of liquid- and vapor phase derivatizations (VP-CD) with TFEH. Peak positions, integration ranges, assignments, and integrated intensities  $B$  of strong infrared bands in TFBA and TFEH, measured in transmission on solutions in tetrachloroethylene, are shown in Table 4. The larger errors in the determination of  $B$  in case of TFEH is caused by the necessity to remove the water from the customary 70-% solution in  $\text{H}_2\text{O}$  by a drying agent. With the  $B$  values and corresponding band areas in ImIRRAS spectra from derivatized samples (see the legends of Figures 10 and 11), functional group densities can be determined using Equation (3).

A frequently observed feature of difference spectra as shown in Figures 10 and 11, obtained by subtracting spectra of untreated samples from spectra taken after derivatization, is the appearance of an inverted or, before offsetting, a negative peak\* in the region below  $1000\text{ cm}^{-1}$ , that is, the region where the aging has its main impact on ImIRRAS spectra during the first hours, see above, Figure 4. It is an obvious conjecture that the reaction with the N-nucleophilic amine and hydrazine, respectively, predominantly attacks electrophilic moieties which were formed in the first  $10^4\text{ s}$  (Figure 6) and that these moieties are in fact epoxy groups for which ring opening by nucleophiles is a characteristic reaction. It is important to note that the aging-related gain of  $928\text{-cm}^{-1}$  band area in the difference spectrum B in Figure 10 (1.32) and the loss of band area upon reaction with TFBA (C,  $-1.30$ ) have virtually the same absolute value,

\*Experiments and simulations show that baseline position, slope and curvature depend on the quality of the optical contact between the IRE and the sample (see Figure 1). Insertion of a 5-nm air gap in the model used above, with  $n_3 = 1.5$ , lowers the baseline absorbance at  $900$  ( $1100$ )  $\text{cm}^{-1}$  by  $0.0015$  ( $0.0021$ ). Therefore, the absolute absorbance in a difference spectrum is normally not a criterion but only the shape of the spectrum. The air gap lowers the band area at  $1000\text{ cm}^{-1}$  by 7%.

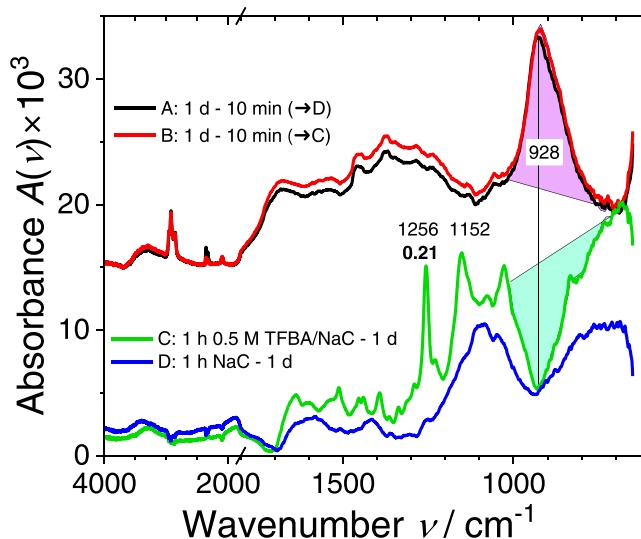


**FIGURE 10** (left) Liquid-phase chemical derivatization (LP-CD) with TFBA: A and B are differences of spectra from two samples from B2 measured at ages of  $t = 10\text{ min}$  and  $1\text{ day}$ , respectively. After  $1\text{ day}$ , samples A and B were treated for  $1\text{ h}$  in a  $0.25\text{ M}$  aqueous solution of  $\text{NaHCO}_3$  (“NaC”) and in an aqueous solution of  $0.5\text{ M}$  4,4,4-trifluorobutylamine (TFBA) and  $0.25\text{ M}$   $\text{NaHCO}_3$ , respectively. D and C are the corresponding difference spectra. Spectra were vertically offset to improve the clarity. Three- or four-digit numbers are locations of band maxima in  $\text{cm}^{-1}$ , the bold number at spectrum C is the band area in  $\text{cm}^{-1}$ . The broad positive (in A and B) or inverted bands (in C and D) with peaks at or near  $928\text{ cm}^{-1}$  have areas (in  $\text{cm}^{-1}$ ) of A: 1.35, B: 1.32, C:  $-1.30$ , D:  $-0.44$ . (The range of integration is indicated by the pink and green areas.)

suggesting that the corresponding functional groups generated by the aging process are quantitatively consumed in the reaction with TFBA. This does not mean, however, that all functional groups are actually binding one molecule of the amine. For the reaction with TFEH, too, the so far unassigned very prominent band with a peak at  $1432\text{ cm}^{-1}$  and a shoulder at  $1468\text{ cm}^{-1}$ , formed in VP derivatization of samples from B1 (black, red, and blue spectra in Figure 11) is not necessarily due to vibrations of the bound  $\text{CF}_3\text{-CH}_2\text{-NH-N=}$  moiety—it could also be due to a side product.

Products of reactions of epoxides with amines and hydrazines, which can be run at low temperatures in water,<sup>[65]</sup> are  $\beta$ -amino alcohols<sup>[66]</sup> and  $\beta$ -hydrazino alcohols,<sup>[67]</sup> respectively. Water<sup>[68]</sup> or  $\text{OH}^-$  anions themselves can also act as nucleophiles and hydrolyze epoxy groups under moderate conditions, resulting in vicinal diols. The appearance of an inverted peak in difference spectrum D in Figure 10 is therefore not surprising. In Figures 10 and 11, the formation of alcohols as well as  $\beta$ -amino and  $\beta$ -hydrazino alcohols, respectively, does not result in the appearance of characteristic sharp peaks due

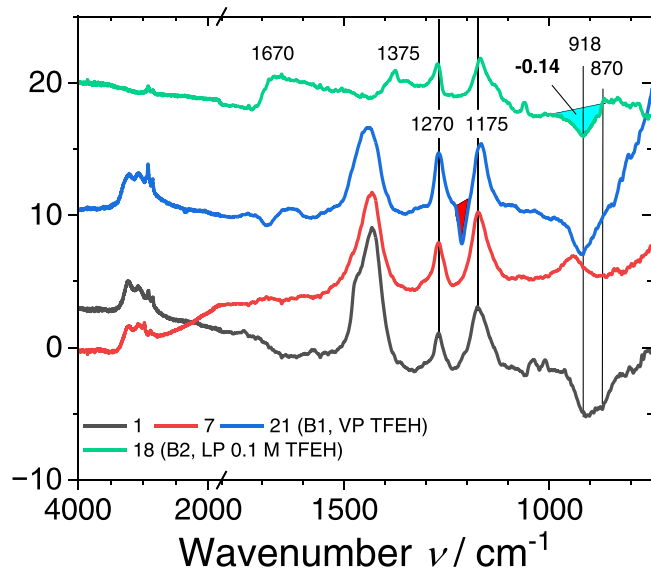


**FIGURE 11** (right) Liquid- and vapor-phase chemical derivatization (LP-, VP-CD) with TEFH: Spectra 1, 7, and 21 are differences of spectra measured on samples from B1 at  $t = 1, 7,$  and 21 days before and after VP-CD with 2,2,2-trifluoro-ethylhydrazine (TFEH), respectively. (The red triangle marks an inverted peak due to a contamination on the underivatized sample.) Spectrum 18 is the difference of spectra measured on a sample from B2 at  $t = 18$  days before and after LP-CD with 0.1 M TFEH in water. Spectra were vertically offset to improve the clarity. Three- or four-digit numbers are locations of band maxima in  $\text{cm}^{-1}$ , the bold number at spectrum 18 is the band area in  $\text{cm}^{-1}$ . Areas with peaks at or near  $1175 \text{ cm}^{-1}$  are 1: 0.21, 7: 0.25, 21: 0.27, 18: 0.14. The broad band between  $1400$  and  $1500 \text{ cm}^{-1}$  in spectra 1, 7, and 21 has a maximum at  $1432 \text{ cm}^{-1}$  and in spectrum 1 a shoulder at  $1468 \text{ cm}^{-1}$ .

**TABLE 4** Integrated intensities  $B$  of  $\text{CF}_3$ -related stretching vibrations in CD reagents TFBA and TFEH.

Reagent	Peak max./ $\text{cm}^{-1}$	Int. range/ $\text{cm}^{-1}$	Ass.	$B/\text{Lmol}^{-1}\text{cm}^{-2}$
TFBA	1254	1284–1224	$\nu_{\text{as}}, \text{CF}_3$	$5200 \pm 5\%$
	1140	1164–1117	$\nu_{\text{s}}, \text{CF}_3$	$3300 \pm 5\%$
TFEH	1297&1261	1335–1220	$\nu_{\text{as}}, \text{CF}_3$	$6300 \pm 10\%$
	1157	1220–1080	$\nu_{\text{s}}, \text{CF}_3$	$12,000 \pm 10\%$

to the C–O–H and N–H moieties because the corresponding vibrational bands are generally only of weak to medium strength or broadened by hydrogen bonding.<sup>[58]</sup> The  $-\text{CF}_3$  groups in TFBA and TFEH, however, allow to detect the presence of these groups with high sensitivity, thanks to the substantial oscillator strength and narrow

band widths of C–F stretching vibrations.<sup>[69,70]</sup> For the evaluation of areal densities  $\rho_n/\text{nm}^{-2}$  Equation (3) was applied with  $f = 53$  (from the empirical equation in Table 2 with ellipsometry results in Section 2.3.1) and integrated intensities  $B$  from Table 4 for antisymmetric and symmetric  $\text{CF}_3$  stretching vibrations in TFBA and TFEH, respectively. Results (numbers per  $\text{nm}^2$ ) are 2.0 and 2.4 for the 1-day and 7-day samples, respectively, from batch B1, 1.3 for the 18-days sample from batch B2 (TFEH derivatization, Figure 11), and 4.6 for the 1-day sample from batch B2 (TFBA derivatization, Figure 10). Process optimizations and more systematic experiments still need to be done to obtain results which can be discussed in terms of derivatization chemistries (amine vs. hydrazine) or methods (liquid vs. vapor phase). For the present paper, it shall suffice to conclude that similar orders of magnitude of  $\rho_n$  are obtained. The results also agree with the expectation that the binding capacity of aging a-C films for N-nucleophiles should not increase substantially beyond an age of 1 day as the functional groups responsible for the reactivity saturate within about  $10^4$  s as suggested by the graph in Figure 6. It must be noted, however, that the stability of amine or hydrazine binding has still to be studied. Preliminary overnight ethanol soaking experiments show that  $\rho_n$  can decrease substantially to below  $1 \text{ nm}^{-2}$ . The good signal-to-noise ratio of the spectra in Figures 10 and 11 allows the expectation that detection limits down to about  $0.1 \text{ nm}^{-2}$  should be possible.

For applications where DLC surfaces are contacting biomolecules, cells, or biological tissues and liquids, an understanding of major aging mechanisms would be very helpful. At present it is an open question, for example, if or to what extent the generation of oxygen functionalities is due to an autoxidation process involving atmospheric  $\text{O}_2$  or possibly to the oxidation by ambient ozone. An autoxidation chain reaction could start with carbon-centered radicals on the fresh DLC surface which are rapidly converted to peroxy radicals in the presence of atmospheric  $\text{O}_2$ <sup>[71]</sup>; the abstraction of hydrogen from C–H bonds by peroxy radicals would generate new C-centered radicals which are immediately scavenged by  $\text{O}_2$  and so forth.<sup>[55]</sup>

The formation of epoxy groups apparently plays no significant role in the oxidative degradation of polymers; in the review by Rabek this kind of oxygen functionality is mentioned not at all.<sup>[55]</sup> There are, however, also kinetic reasons to exclude the formation of electrophilic groups via the outlined autoxidation mechanism via hydroperoxy groups: Hydrogen abstraction by a peroxy radical requires the presence of surface C–H groups and sufficient mobility of at least one of the reaction partners. While the H content of the studied

films is not known, sufficient mobility on the rigid a-C surface could be lacking. More importantly, with an activation energy of at least 110 kJ/mol<sup>[72]</sup> the unimolecular thermal decomposition rate of hydroperoxides at room temperature is many (at least about 7) orders of magnitude too small to explain the observed time constant of 2300 s (see Figure 6). Metastable hydroperoxides themselves can be excluded as amine- or hydrazine-binding functional groups: Amines are known to reduce hydroperoxides to alcohols nearly quantitatively.<sup>[73]</sup> The reactions with hydrazines, too, result mainly in reduction.<sup>[74]</sup>

A more likely alternative route toward epoxy groups is opened by the presence of extended graphene- or PAH-like domains of sp<sup>2</sup>-bonded carbon atoms in a-C films<sup>†</sup>: Multinuclear aromatics can autoxidize without the participation of hydrogen.<sup>[76]</sup> In their study of a range of coal chars, Levi et al. were led to conclude that epoxidation is the prevalent type of oxygen functionalization by molecular oxygen at room temperature.<sup>[77]</sup> Mechanisms of O<sub>2</sub> chemisorption and the evolution of functional groups on graphene are part of an actively developing area of research.<sup>[78]</sup> In independent theoretical calculation it was consistently found that vacancy defects in graphite (0001) surfaces,<sup>[79]</sup> graphene sheets,<sup>[80,81]</sup> and CNTs<sup>[81]</sup> lower the energy barrier for dissociative chemisorption drastically, for example, from 270 kJ/mol for defect-free graphene to less than 30 kJ/mol for a single-vacancy defect. Low-energy ion bombardment is known to induce defects in graphene sheets.<sup>[82]</sup> In earlier studies on O<sub>2</sub> chemisorption on graphite, it was already noticed that, at 300°C, basal graphite surfaces bombarded with 500-eV neon ions were seven orders of magnitude more reactive than nonbombarded edge surfaces<sup>[83]</sup> (see also Barber et al.<sup>[84]</sup>). During DLC film growth by sputtering, particles with energies of typically 100 eV or more are bombarding the films surface. Even in the absence of a negative bias voltage applied to the substrate, backscattering of neutralized sputter gas ions from the target provides a substantial influx of energetic, potentially defect-producing particles.<sup>[85]</sup> Therefore, it is obvious that structures similar to vacancy defects in graphene sheet are also involved in epoxy group formation on DLC upon O<sub>2</sub> chemisorption. It should be noted that, aside from epoxy groups, cyclic ether groups with larger rings play important roles as intermediates or products of O<sub>2</sub> chemisorption in theoretical calculations.

<sup>†</sup>In comparing the extended clusters of sp<sup>2</sup>-hybridized carbon atoms in DLC with PAHs or graphene, it must be noted that there is an essential difference in electronic properties between the latter, which is crucial for the chemical interaction with O<sub>2</sub>. The difference is due to the lack of hydrogen saturation of C atoms at graphene edges.<sup>[75]</sup>

It is an interesting open question to what extent such ethers may contribute to chemical reactions with nucleophiles.

While the defect-induced uptake of O<sub>2</sub> represents a convincing explanation of the rapid generation of electrophilic groups on a-C, it cannot be excluded that ozone in the ambient air contributes to the oxidation, too: Polycyclic aromatic hydrocarbons adsorbed on solid surfaces such as silica, graphite or (filter) paper are known to be susceptible to oxidation by ozone at ambient-level concentrations.<sup>[86–88]</sup> The decay of surface coverage by the PAHs is generally exponential in time and proportional to the O<sub>3</sub> concentration. Even in only 0.2 ppm O<sub>3</sub>, half-lives of perylene and benzo[a]pyrene adsorbed on fused silica as low as 132 and 2.6 min were reported.<sup>[86]</sup> With measured second-order rate coefficients in the range of 1 × 10<sup>-16</sup> to 1 × 10<sup>-17</sup> cm<sup>3</sup>s<sup>-1</sup>, these reactions are much faster than most comparable gas-phase reactions.<sup>[88]</sup> The attack of soot platelets or PAHs by ozone and subsequent loss of O<sub>2</sub>, resulting in epoxy and oxepine moieties, has also been studied theoretically.<sup>[89,90]</sup>

In view of a seven orders of magnitudes higher O<sub>2</sub> content in typical indoor air<sup>[91]</sup> and the low barrier for defect-induced chemisorption of O<sub>2</sub>, however, it is questionable if the oxidation of sputtered a-C by O<sub>3</sub> actually can compete with the chemisorption of O<sub>2</sub>.

In the above-cited ref.<sup>[83]</sup> the reactive adsorption coefficient of water on ion-bombarded graphite was found to be smaller than the corresponding value for O<sub>2</sub> by more than a factor of 10<sup>5</sup> (at 30°C and an oxygen coverage of 0.5). According to theoretical calculations, barriers of 154 and 19 kJ/mol were determined for chemisorption of H<sub>2</sub>O and O<sub>2</sub>, respectively, at vacancies on the graphite (0001) surface.<sup>[79]</sup> Therefore, the typical 1-% H<sub>2</sub>O fraction of the indoor air in the experiments is not expected to play an important role in the first reaction steps.

In general, it is not possible to represent graphene, its defects and oxidation products graphically like classical Kekulé molecules. To get an impression of the molecular environment of epoxy groups in oxidized graphene, the reader is recommended to look at the models of Lorf-Klinowski, Dékány and Hofmann in the first figure of the cited review article on GO.<sup>[25]</sup>

## 4 | CONCLUSIONS AND OUTLOOK

The application of ImIRRAS to study surface functional groups produced spontaneously during aging of nominally H-free amorphous DLC coatings (a-C) exposed to ambient laboratory air allows to gain insights into surface-chemical processes which are not easily

accessible by XPS. Within the first  $10^4$  s (about 3 h) after venting the load lock of the sputter apparatus used to deposit the films, the growth of a vibrational band peaking at  $928\text{ cm}^{-1}$  virtually comes to an end, attributed to the generation of epoxy groups. There are two main arguments for this assignment: (1) Peak positions of band components which can be identified in the second derivative of spectra are characteristic for symmetric and asymmetric deformation vibrations of the epoxy ring. (2) Upon contact with vapors or aqueous solutions of two selected N-nucleophiles, TFBA and TFEH, partial or virtually complete vanishing of the band is observed, due to ring opening. Comparing band areas of  $\text{CF}_3$  stretching vibrations in ImIRRAS spectra with corresponding integrated intensities  $B$  of the reagents enables measurements of number densities  $\rho_n$  of reagent molecules physisorbed or chemisorbed on the film surface. Values of  $\rho_n$  between 1 and 5 per  $\text{nm}^2$  were measured in the present study for film ages of 1 day or beyond. The sensitivity of ImIRRAS allows the quantification of functional groups with high oscillator strength down to areal densities in the lower  $0.1\text{-nm}^{-2}$  range. Thus it can be shown that the density of carbonyl groups is still quite small, about  $0.3\text{ nm}^{-2}$  after 150 min, when the epoxy group formation is nearly completed, but it grows substantially within the following 24 h.

Compared with graphite or graphene, clusters of  $\text{sp}^2$ -hybridized C atoms in a-C represent a highly defective form of carbon. Therefore, in view of previous experimental and theoretical evidence in reports on defect-induced interaction of these materials with  $\text{O}_2$ , the observed rapid formation of electrophilic oxygen-functional groups on a-C surfaces by chemisorption of molecular oxygen from the open air is not surprising. So far, however, a participation of ambient ozone and water vapor cannot be excluded. A study of the effects of different storage conditions is planned in the near future, including a comparison of ImIRRAS results with elemental analyses by XPS. Another open question to be investigated is the role of hydrogen atoms incorporated in the DLC film, for example from water vapor in the residual gas in the case of nominally H-free a-C films, or from hydrocarbons in the process gas, as in a-C:H films prepared by PACVD. Last, but not least, to know and understand the temporal evolution of functional group densities on the time scale of 100 days is of interest, not only from the scientific point of view but also for applications.

## ACKNOWLEDGMENTS

The authors acknowledge funding of their work by the Deutsche Forschungsgemeinschaft (DFG, GZ: KL 1096/35-1). They thank their colleagues of IOT Ezgi Melis Dogan-Guner, Meret Leonie Betz, Lars Bröcker, and Axel

Pregizer-Winter for helpful discussions and technical assistance.

## DATA AVAILABILITY STATEMENT

The data that support the findings of this study are available from the corresponding author upon reasonable request.

## ORCID

Claus-Peter Klages  <http://orcid.org/0000-0001-5678-5845>

## REFERENCES

- [1] C. A. Love, R. B. Cook, T. J. Harvey, P. A. Dearnley, R. J. K. Wood, *Tribol. Int.* **2013**, 63, 141. <https://doi.org/10.1016/j.triboint.2012.09.006>
- [2] P. Martin, *Medical Coatings and Deposition Technologies* (Eds: D. A. Glocker, S. V. Ranade), John Wiley & Sons, Inc. Hoboken, NJ, and Scrivener Publishing LLC, Salem, MA, USA **2016**, pp. 181.
- [3] A. M. Trimukhe, K. N. Pandiyaraj, A. Tripathi, J. S. Melo, R. R. Deshmukh, *Advances in Biomaterials for Biomedical Applications* (Eds: A. Tripathi, J. S. Melo), Springer Nature, Singapore Pte Ltd., **2017**, pp. 95.
- [4] M. Rahmati, M. Mozafari, *Front. Bioeng. Biotechnol.* **7** **2019**, pp. 4. <https://doi.org/10.3389/fbioe.2019.00004>
- [5] R. Ganesan, B. Akhavan, M. A. Hiob, D. R. McKenzie, A. S. Weiss, M. M. M. Bilek, *Carbon* **2018**, 139, 118. <https://doi.org/10.1016/j.carbon.2018.06.024>
- [6] Y. Zhang, C. Chai, X. S. Jiang, S. H. Teoh, K. W. Leong, *Mater. Sci. Eng.* **2007**, 27, 213. <https://doi.org/10.1016/j.msec.2006.03.013>
- [7] H. Ishige, S. Akaike, T. Hayakawa, M. Hiratsuka, Y. Nakamura, *Dent. Mater. J.* **2019**, 38, 424. <https://doi.org/10.4012/dmj.2018-060>
- [8] H. J. Steffen, J. Schmidt, A. Gonzalez-Elipse, *Surf. Interface Anal.* **2000**, 29, 386. [https://doi.org/10.1002/1096-9918\(200006\)29:6%3C386::AID-SIA882%3E3.0.CO;2-0](https://doi.org/10.1002/1096-9918(200006)29:6%3C386::AID-SIA882%3E3.0.CO;2-0)
- [9] D. S. Everhart, C. N. Reilley, *Anal. Chem.* **1981**, 53, 665. <https://doi.org/10.1021/ac00227a022>
- [10] D. S. Everhart, C. N. Reilley, *Surf. Interface Anal.* **1981**, 3, 126. <https://doi.org/10.1002/sia.740030306>
- [11] D. S. Everhart, C. N. Reilley, *Surf. Interface Anal.* **1981**, 3, 258. <https://doi.org/10.1002/sia.740030606>
- [12] N. Takahashi, H. Mori, Y. Kimoto, T. Ohmori, A. Murase, *Hyomen Kagaku* **2005**, 26, 492 (in Japanese).
- [13] N. Takahashi, *R&D Rev Toyota CRDL.* **2006**, 41(1), 52.
- [14] H. Kondo, Y. Nishida, *Bull. Chem. Soc. Jpn.* **2007**, 80, 1405. <https://doi.org/10.1246/bcsj.80.1405>
- [15] S. Takabayashi, K. Okamoto, H. Sakaue, T. Takahagi, K. Shimada, T. Nakatani, *J. Appl. Phys.* **2008**, 104, 043512. <https://doi.org/10.1063/1.2969792>
- [16] S. Takabayashi, K. Okamoto, H. Motoyama, T. Nakatani, H. Sakaue, T. Takahagi, *Surf. Interface Anal.* **2010**, 42, 77. <https://doi.org/10.1002/sia.3156>
- [17] M. Yang, M. J. Marino, V. J. Bojan, O. L. Eryilmaz, A. Erdemir, S. H. Kim, *Appl. Surf. Sci.* **2011**, 257, 7633. <https://doi.org/10.1016/j.apsusc.2011.03.152>

- [18] M. Cloutier, C. Harnagea, P. Hale, O. Seddiki, F. Rosei, D. Mantovani, *Diamond Relat. Mater.* **2014**, *48*, 65. <https://doi.org/10.1016/j.diamond.2014.07.002>
- [19] S. Bachmann, M. Schulze, J. Morasch, S. Hesse, L. Hussein, L. Krell, J. Schnagl, R. W. Stark, S. Narayan, *Appl. Surf. Sci.* **2016**, *371*, 613. <https://doi.org/10.1016/j.apsusc.2016.02.192>
- [20] J. Robertson, *Diamond Relat. Mater.* **1997**, *6*, 212. [https://doi.org/10.1016/S0925-9635\(96\)00627-9](https://doi.org/10.1016/S0925-9635(96)00627-9)
- [21] S. Kaciulis, *Surf. Interface Anal.* **2012**, *44*, 1155. <https://doi.org/10.1002/sia.4892>
- [22] Y. Liu, J. Liggiio, S.-M. Li, D. Breznan, R. Vincent, E. M. Thomson, P. Kumarathasan, D. Das, J. Abbatt, M. Antiñolo, L. Russell, *Environ. Sci. Technol.* **2015**, *49*, 2806. <https://doi.org/10.1021/es505298d>
- [23] Y. Liu, H. Jiang, C. Liu, Y. Ge, L. Wang, B. Zhang, H. He, S. Liu, *Atmospheric Chemistry and Physics* **2019**, *19*, 8175. <https://doi.org/10.5194/acp-19-8175-2019>
- [24] C. A. Barrios, V. Canalejas-Tejero, *Nanoscale* **2015**, *7*, 3435. <https://doi.org/10.1039/c4nr06271j>
- [25] P. P. Brisebois, M. Siaz, *J. Mater. Chem. C* **2020**, *8*, 1517. <https://doi.org/10.1039/C9TC03251G>
- [26] P. I. Kazaryan, S. V. Avakyan, S. Simonyan, A. A. Gevorkyan, *Chem. Heterocycl. Compds.* **1990**, *26*, 146. <https://doi.org/10.1007/BF00499406>
- [27] S. D. Stamatov, J. Stawinski, *Tetrahedron* **2005**, *61*, 3659. <https://doi.org/10.1016/j.tet.2005.02.034>
- [28] J. M. Tedder, *Chem. Rev.* **1955**, *55*, 787. <https://doi.org/10.1021/cr50005a001>
- [29] D. Briggs, C. R. Kendall, *Int. J. Adhes. Adhes.* **1982**, *2*, 13. [https://doi.org/10.1016/0143-7496\(82\)90061-6](https://doi.org/10.1016/0143-7496(82)90061-6)
- [30] L. J. Gerenser, J. F. Elman, M. G. Mason, J. M. Pochan, *Polymer* **1985**, *26*, 1162. [https://doi.org/10.1016/0032-3861\(85\)90245-9](https://doi.org/10.1016/0032-3861(85)90245-9)
- [31] L. J. Gerenser, J. F. Elman, M. G. Mason, J. M. Pochan, *Polymer* **1985**, *26*, 1162. [https://doi.org/10.1016/0032-3861\(86\)90072-8](https://doi.org/10.1016/0032-3861(86)90072-8)
- [32] A. Chilkoti, B. D. Ratner, D. Briggs, *Chem. Mater.* **1991**, *3*, 51. <https://doi.org/10.1021/cm00013a016>
- [33] I. Sutherland, E. Sheng, D. M. Brewis, R. J. Heath, *J. Mater. Chem.* **1994**, *4*, 683. <https://doi.org/10.1039/JM9940400683>
- [34] R. P. Papat, I. Sutherland, E. S. Sheng, *J. Mater. Chem.* **1995**, *5*, 713. <https://doi.org/10.1039/JM9950500713>
- [35] V. I. Povstugar, S. S. Mikhailova, A. A. Shakov, *J. Anal. Chem. (Transl. of Zh. Anal. Khim.)* **2000**, *55*, 405. <https://doi.org/10.1007/BF02757474>
- [36] A. Y. Rulev, *Russ. Chem. Rev.* **2011**, *80*, 197. <https://doi.org/10.1070/RC2011v080n03ABEH004162>
- [37] Y. Liu, G. He, B. Chu, Q. Ma, H. He, *Fundam. Res.* **2023**, *3*, 579. <https://doi.org/10.1016/j.fmre.2022.02.012>
- [38] M. Ilić, F.-H. Haegel, A. Lolić, Z. Nedić, T. Tosti, I. S. Ignjatović, A. Linden, N. D. Jablonowski, H. Hartmann, *PLoS One* **2022**, *17*, e0277365. <https://doi.org/10.1371/journal.pone.0277365>
- [39] V. P. Tolstoy, L. V. Chernyshova, V. A. Skryshevsky, *Handbook of infrared spectroscopy of ultrathin films*, Wiley-Interscience, John Wiley & Sons, Inc, Hoboken, NJ, USA **2003**.
- [40] N. J. Harrick, A. I. Carlson, *Appl. Opt.* **1971**, *10*, 19. <https://doi.org/10.1364/AO.10.000019>
- [41] A. S. Wexler, *Appl. Spectrosc. Rev.* **1967**, *1*, 29. <https://doi.org/10.1080/05704926708547581>
- [42] J. D. E. McIntyre, D. E. Aspnes, *Surf. Sci.* **1971**, *24*, 417. [https://doi.org/10.1016/0039-6028\(71\)90272-X](https://doi.org/10.1016/0039-6028(71)90272-X)
- [43] Y. J. Chabal, *Surf. Sci. Rep.* **1988**, *8*, 211. [https://doi.org/10.1016/0167-5729\(88\)90011-8](https://doi.org/10.1016/0167-5729(88)90011-8)
- [44] J. D. E. McIntyre, *Optical Properties of Solids—New Developments* (Ed: B. O. Seraphin), North-Holland Publishing Company, Amsterdam **1976**, pp. 555.
- [45] M. A. Ordal, R. J. Bell, R. W. Alexander Jr., L. L. Long, M. R. Querry, *Appl. Opt.* **1985**, *24*, 4493. <https://doi.org/10.1364/AO.24.004493>
- [46] J. Brandrup, E. H. Immergut, E.-A. Grulke, *Polymer Handbook*, 4th ed., John Wiley & Sons, Ltd., Chichester **1999**.
- [47] N. Savvides, *J. Appl. Phys.* **1986**, *59*, 4133. <https://doi.org/10.1063/1.336672>
- [48] J. Knoll, J. Geiger, *Phys. Rev. B: Condens. Matter Mater. Phys.* **1984**, *29*, 5651. <https://doi.org/10.1103/PhysRevB.29.5651>
- [49] M. Smith, L. Scudiero, J. Espinal, J.-S. McEwen, M. Garcia-Perez, *Carbon* **2016**, *110*, 155. <https://doi.org/10.1016/j.carbon.2016.09.012>
- [50] A. Kovtun, D. Jones, S. Dell'Elce, E. Treossi, A. Liscio, V. Palermo, *Carbon* **2019**, *143*, 268. <https://doi.org/10.1016/j.carbon.2018.11.012>
- [51] D. J. Morgan, C—*J. Carbon Res.* **2021**, *7*, 51. <https://doi.org/10.3390/c7030051>
- [52] T. R. Gengenbach, G. H. Major, M. R. Linford, C. D. Easton, *J. Vac. Sci. Technol., A* **2021**, *39*, 013204. <https://doi.org/10.1116/6.0000682>
- [53] B. Moeini, M. R. Linford, N. Fairley, A. Barlow, P. Cumpson, D. Morgan, V. Fernandez, J. Baltrusaitis, *Surf. Interface Anal.* **2022**, *54*, 67. <https://doi.org/10.1002/sia.7021>
- [54] M. C. Biesinger, *Appl. Surf. Sci.* **2022**, *597*, 153681. <https://doi.org/10.1016/j.apsusc.2022.153681>
- [55] J. F. Rabek, *Degradation of Polymers* (Eds: C. H. Bamford, C. F. H. Tipper), Comprehensive Chemical Kinetics, Vol. 14, Elsevier Scientific Publishing Company, Amsterdam, Oxford, New York **1975**, pp. 425–538. [https://doi.org/10.1016/S0069-8040\(08\)70336-4](https://doi.org/10.1016/S0069-8040(08)70336-4)
- [56] S.-C. Seo, D. C. Ingram, H. H. Richardson, *J. Vac. Sci. Technol., A* **1995**, *13*, 2856. <https://doi.org/10.1116/1.579604>
- [57] L. G. Jacobsohn, F. L. Freire Jr., *J. Vac. Sci. Technol., A* **1999**, *17*, 2841. <https://doi.org/10.1116/1.582022>
- [58] G. Socrates, *Infrared and Raman Characteristic Group Frequencies*, John Wiley & Sons, Chichester, England **2001**.
- [59] A. Sadat, I. J. Joye, *Appl. Sci.* **2020**, *10*, 5918. <https://doi.org/10.3390/app10175918>
- [60] C.-P. Klages, A. Jung, M. L. Betz, V. Raev, *Plasma Chem. Plasma Process.* **2023**, *43*, 933. <https://doi.org/10.1007/s11090-023-10352-9>
- [61] R. Brendel, D. Bormann, *J. Appl. Phys.* **1992**, *71*, 1. <https://doi.org/10.1063/1.350737>
- [62] R. A. Nyquist, *Appl. Spectrosc.* **1986**, *40*, 275. <https://opg.optica.org/as/abstract.cfm?URI=as-40-2-275>
- [63] A. Rosowsky, *Chemistry of Heterocyclic Compounds*, 19 (Ed: A. Weissberger), John Wiley & Sons, Ltd., New York and London, **1964**, pp. 8.
- [64] J. Bomstein, *Anal. Chem.* **1958**, *30*, 544. <https://doi.org/10.1021/ac60136a029>

- [65] S. Bonollo, D. Lanari, L. Vaccaro, *Eur. J. Org. Chem.* **2011**, 2587. <https://doi.org/10.1002/ejoc.201001693>
- [66] N. Azizi, M. R. Saidi, *Org. Lett.* **2005**, 7, 3649. <https://doi.org/10.1021/ol051220q>
- [67] Z. Zalan, L. Lazar, F. Fulop, *Curr. Org. Chem.* **2005**, 9, 357. <https://doi.org/10.2174/1385272053174949>
- [68] Z. Wang, Y.-T. Cui, Z.-B. Xu, J. Qu, *J. Org. Chem.* **2008**, 73, 2270. <https://doi.org/10.1021/jo702401t>
- [69] D. F. Harnish, R. P. Hirschmann, *Appl. Spectrosc.* **1970**, 24, 28. <https://opg.optica.org/as/abstract.cfm?URI=as-24-1-28>
- [70] V. F. Kalasinsky, H. V. Anjaria, *J. Phys. Chem.* **1980**, 84, 1940. <https://doi.org/10.1021/j100452a015>
- [71] F. Khelifa, S. Ershov, Y. Habibi, R. Snyders, P. Dubois, *Chem. Rev.* **2016**, 116, 3975. <https://doi.org/10.1021/acs.chemrev.5b00634>
- [72] J. R. Thomas, *J. Am. Chem. Soc.* **1955**, 77, 246. <https://doi.org/10.1021/ja01606a091>
- [73] C. W. Capp, E. G. E. Hawkins, *J. Chem. Soc.* **1953**, 4106. <https://doi.org/10.1039/JR9530004106>
- [74] K. Maruyama, T. Otsuki, T. Iwao, *J. Org. Chem.* **1967**, 32, 82. <https://doi.org/10.1021/jo01277a021>
- [75] L. R. Radovic, *Carbon* **2021**, 171, 798. <https://doi.org/10.1016/j.carbon.2020.09.054>
- [76] N. Montoya Sánchez, A. de Klerk, *Appl. Petrochem. Res.* **2018**, 8, 55. <https://doi.org/10.1007/s13203-018-0199-4>
- [77] G. Levi, O. Senneca, M. Causà, P. Salatino, P. Lacovig, S. Lizzit, *Carbon* **2015**, 90, 181. <https://doi.org/10.1016/j.carbon.2015.04.003>
- [78] V. A. Nebol'sin, V. Galstyan, Y. E. Silina, *Surf. Interfaces* **2020**, 21, 100763. <https://doi.org/10.1016/j.surfin.2020.100763>
- [79] A. Allouche, Y. Ferro, *Carbon* **2006**, 44, 3320. <https://doi.org/10.1016/j.carbon.2006.06.014>
- [80] J. M. Carlsson, F. Hanke, S. Linic, M. Scheffler, *Phys. Rev. Lett.* **2009**, 102, 166104. <https://doi.org/10.1103/PhysRevLett.102.166104>
- [81] Z. Fang, L. Li, D. A. Dixon, R. R. Fushimi, E. J. Dufek, *J. Phys. Chem. C* **2021**, 125, 20686. <https://doi.org/10.1021/acs.jpcc.1c06741>
- [82] P. Ahlberg, F. O. L. Johansson, Z.-B. Zhang, U. Jansson, S.-L. Zhang, A. Lindblad, T. Nyberg, *APL Mater.* **2016**, 4, 046104. <https://doi.org/10.1063/1.4945587>
- [83] S. R. Kelemen, H. Freund, *Carbon* **1985**, 23, 619. [https://doi.org/10.1016/0008-6223\(85\)90221-0](https://doi.org/10.1016/0008-6223(85)90221-0)
- [84] M. Barber, E. L. Evans, J. M. Thomas, *Chem. Phys. Lett.* **1973**, 18, 423. [https://doi.org/10.1016/0009-2614\(73\)80208-8](https://doi.org/10.1016/0009-2614(73)80208-8)
- [85] H. F. Winters, H. J. Coufal, W. Eckstein, *J. Vac. Sci. Technol., A* **1993**, 11, 657. <https://doi.org/10.1116/1.578787>
- [86] C.-H. Wu, I. Salmeen, H. Niki, *Environ. Sci. Technol.* **1984**, 18, 603. <https://doi.org/10.1021/es00126a007>
- [87] J. N. Pitts Jr., H.-R. Paur, B. Zielinska, J. Arey, A. M. Winer, T. Ramdahl, V. Mejia, *Chemosphere* **1986**, 15, 675. [https://doi.org/10.1016/0045-6535\(86\)90033-0](https://doi.org/10.1016/0045-6535(86)90033-0)
- [88] E. Perraudin, H. Budzinski, E. Villenave, *J. Atmos. Chem.* **2006**, 56, 57. <https://doi.org/10.1007/s10874-006-9042-x>
- [89] A. Maranzana, G. Serra, A. Giordana, G. Tonachini, G. Barco, M. Causà, *J. Phys. Chem. A* **2005**, 109, 10929. <https://doi.org/10.1021/jp053672q>
- [90] A. Giordana, A. Maranzana, G. Ghigo, M. Causà, G. Tonachini, *J. Phys. Chem. A* **2008**, 112, 973. <https://doi.org/10.1021/jp075487d>
- [91] C. J. Weschler, *Indoor Air* **2000**, 10, 269. <https://doi.org/10.1034/j.1600-0668.2000.010004269.x>

**How to cite this article:** C.-P. Klages, R. Bandorf, H. Gerdes, A. Jung, V. Raev, *Plasma. Process. Polym.* **2023**, e2300123. <https://doi.org/10.1002/ppap.202300123>